LAYING THE FOUNDATION FOR AN ARTIFICIAL NEURAL NETWORK FOR PHOTOGRAMMETRIC RIVERINE BATHYMETRY

Elena Belcore [1 *]; Vincenzo Di Pietra[1]

[1]Politecnico di Torino, DIATI, Department of Environment, Land and Infrastructure Engineering. Corso Duca degli Abruzzi, 24, 10129 Torino, Italia- Email(s): elena.belcore@polito.it; vincenzo.dipietra@polito.it

Commission IV, WG IV/4

KEY WORDS: UAS, Riverine bathymetry, submerged topography, artificial intelligence, artificial neural network, channel morphology, SfM, Python, Digital Twin Earth.

ABSTRACT:

This work aims to test the effectiveness of artificial intelligence for correcting water refraction in shallow inland water using very high-resolution images collected by Unmanned Aerial Systems (UAS) and processed through a total FOSS workflow. The tests focus on using synthetic information extracted from the visible component of the electromagnetic spectrum. An artificial neural network is created using data of three morphologically similar alpine rivers. The RGB information, the SfM depth and seven radiometric indices are calculated and stacked in an 11-bands raster (input dataset). The depths are calculated as the difference between the Up component of the bathymetry cross-sections and the water surface quotas and constitute the dependent variable of the regression. The dataset is then scaled. The observations of one of the analyzed case studies are used as the unseen dataset to test the generalization capability of the model. The remaining observations are divided into test (20%) and training (80%) datasets. The generated NN is a 3-layer MLP model with one hidden layer and the Rectified Linear Unit (ReLU) and sigmoid activation functions. The weights are initialized to small Gaussian random values, and kernel regularizers, L1 and L2, are added to reduce the overfitting. Weights are updated with the Adam search technique, and the mean squared error is the loss function. The importance and significance of 11 variables are assessed. The model has a 0.70 r-squared score on the test dataset and 0.77 on the training dataset. The MAE is 0.06 and the RMSE 0.08, similar results obtained from the unseen dataset. Although the good metrics, the model shows some difficulties generalizing swallow depths.

1. INTRODUCTION

The optimism and enormous potentialities regarding remote sensing (RS) in river research were already evident in 2009 when Legleiter stated how new earth observation techniques would provide extensive, quantitative data that could yield insight into the organization of fluvial systems (Legleiter et al., 2009). One of the emerging applications of RS in fluvial studies is in bathymetry. The submerged topography is a crucial variable in fluvial processes and hydrodynamics models. Typically, bathymetry measures are realized using echo sounders embedded on vessels; traditional topographic surveys with total stations and Real-time Kinematic Positioning (RTK-GNSS) are also applied in streams, riverbeds and dry riverbeds. Besides being time-consuming and often limited in the spatial scale, traditional data collection is strongly limited by currents and water depth (such as shallow mountain streams and deep waters) (Dietrich, 2017; Burgazzi et al., 2021). In such a scenario, RS has progressively complemented traditional methods, providing high-resolution information from laser scanning and optical sensors, which have been recently mounted on unmanned aerial vehicles (UAV) systems (Mancini et al., 2020; Vélez-Nicolás et al., 2021). UAVs, also known as unmanned aerial systems (UAS), remotely piloted aircraft systems (RPAS) or drones, have emerged as new means for environmental monitoring and management. UAVs can be embedded with a wide range of sensors. The application of UAVs in river bathymetry, and more generally, in hydrology, has been analyzed by several authors (Ioli et al., 2020; Vélez-Nicolás et al., 2021) provide extensive surveys on the current literature on the theme.

Regardless of the means carrying the sensors, imaging sensors can play a key role in gaining spatial and temporal insight into fluvial morphology conditions. The main obstacle in optical-derived bathymetry is the refraction of the light passing the atmosphere-water interface. The refraction distorts the photogrammetric scene reconstruction, generally manifested as in-water measures to be underestimated (i.e., shallower than reality). Several attempts to correct the water refraction-derived distortions have been made in the literature. They can be categorized according to their nature: Radiometric-based and Photogrammetry-based methods.

Photogrammetry-, or geometry-, based methods consider that any photo of water captured by an optical sensor is affected by refraction, the bending of the light as it passes from the atmosphere to the water, which is affected by water turbidity, depth and the variability of the light conditions (Balletti et al., 2015; Calantropio et al., 2021). The refraction causes the photogrammetry depth measures (i.e., Up component) of the riverbed to be shallower than the actual one. The photogrammetric-based methods aim to define the difference between the apparent depth (ha) and actual depth (h) considering the refraction angles (Θ1, Θ2), the apparent riverbed measure from the photogrammetric process, and the camera acquisition point.

Radiometric methods are centred on the spectral response of the means crossed by the light and are typically built on the theory that the total radiative energy reflected by the water column is function of the water depth (Makboul et al., 2017). Mainly, these methods aim to attenuate the electromagnetic wave in the water column and the reflection from the bottom of the water body (Vélez-Nicolás et al., 2021), which is generally modelled with

* Corresponding author

the Beer-Lambert Law (Lyzenga, 1978; Stumpf et al., 2003). Usually, they are empirical methods that use the riverbed measures realized with GNSS receivers (Carbonneau et al., 2006), multi/single beam echo sounders (Vélez-Nicolás et al., 2021) and recently with LiDAR data (Pontoglio et al., 2020; Mandlburger et al., 2021). A separate group should be dedicated to the green LiDAR, a relatively new instrument that can perform direct bathymetry (i.e., no need for corrections); nevertheless, because it is not the goal of this work, it is not analyzed.

Indeed radiometric approaches have been well established and broadly applied since the 2000s. The first applications used satellite and topography information to find the function that described the relationship between water depth and reflectance through regressions. The first attempts were made on coastal areas using satellite imagery and successively on rivers (Carbonneau et al., 2006). In airborne imagery, the high spectral variability characterizing the elements of riverbeds and seabeds impacts the regression models negatively. A solution to this problem was proposed by (Geyman et al., 2019), who developed a clustered approach for the bathymetry of variable seabeds.

Inaccuracies of depth mapping derived from spectral heterogeneity of sea and riverbeds are exacerbated for very high spatial resolution (VHR) data. With the diffusion of UAS systems, the availability of VHR datasets has increased. Woodget's bathymetry method from UAS (Woodget et al., 2015) was one of the first works focused on the topic. Many researchers address their work on UAV bathymetry. For example (Rossi et al., 2020) introduced the concept of UAV-Derived Bathymetry (UDB) and corrected the water refraction from UAS by applying Lyzenga's correction method (Lyzenga, 1978). Nevertheless, the most recent UAS-based bathymetry works use machine learning (ML) to correct the water refraction. (Agrafiotis et al., 2019) proposed a Support Vector Machine (SVM)-based bathymetry from UAS. Similarly, (Slocum et al., 2020) proposed a combined geometric, radiometric, and neural network approach for mapping the submerged topography of shallow rivers using RGB sensors.

Additional analysis is required on the introduction of ML in river and sea bathymetry. If ten years ago, the primary goal of the research on submerged topography was to understand the relation between the water column reflectance and the water depth using statistical and trigonometrical models, the spread of artificial intelligence that allows users to investigate the non-linear and very complex relationship between variables, has given a new light of interest on spectral-based bathymetry. (Wang et al., 2007) are the forerunners of neural networks applied to water depth studies, followed closely by much other research based on satellite data (Makboul et al., 2017; Kaloop et al., 2021) and UAV (Slocum et al., 2020). Although these efforts provided good results, there are some concerns regarding the applicability of ML for bathymetry problems since the performance of learning-based techniques can be only as good as the training data.

Research to date has done little regarding UAS-based bathymetric estimation via Artificial Intelligence. Many authors computed band ratios, which are considered particularly effective in radiometric-based bathymetry. Most band ratios are focused on the visible portion of the electromagnetic spectrum that is thought more significant in water depth estimation. Also, most of the analyzed studies are tested over lakes, coastal areas and big rivers. The river ecosystem is a complex scenario composed of the whole aquatic environment of the river, i.e., its non-living part (water, rocks, infrastructure, etc.) and the aquatic animal and plant organisms living in it (algae, aquatic plants, insects, etc.). From this, the complexity of the radiometric response in shallow river stretches, compared with that in lakes and coastal areas, is evident. The presence of plant organisms on the bottom, and the different grain sizes of the bottom material due to current velocity and turbulence in different stretches (upland, valley bottom and lowland), negatively affect methodologies based on spectral response attenuation. The primary focus of this study is on shallow (<1 m deep) and clearly flowing streams where substrate variability could have a pronounced effect on depth retrieval. In particular, valley bottom sections of alpine rivers in Piedmont are analyzed.

This work aims to test the effectiveness of radiometric empirical methods based on artificial neural networks to correct water refraction in shallow inland water using UAS data. Particularly, the method focuses on using information generated through Structure from Motion (SfM), which provides information related to the terrain and riverbed morphology. The results of the models were compared using the coefficient of determination and the mean squared error.

The following sections will present the methodology for bathymetry extraction from UAV photogrammetric products by reviewing a customized ANN model trained on samples related to three Piedmont alpine rivers. The data acquisition and preparation for the Dora Riparia, Orco and Pellice rivers will be described, and the results will be discussed.

2. METHODS

This section presents dataset acquisition, feature extraction, preprocessing and the structure of the NN models, including the training procedure with respect to the case studies described in Section 3.

The proposed method for river bathymetry extraction exploits the well-documented benefits of artificial neural networks in analyzing heterogeneous spatial information and, in particular, very high-resolution photogrammetric products. The dataset array prepared as input for the network is a set of radiometric and geometric features associated with in-water and ground georeferenced points. These points belong to river cross-sections whose depths were measured by independent techniques with high accuracy (GNSS geodetic survey and Acoustic Doppler Current Profiler). The points of the bathymetry cross-section constituted the so-called "Depth_real" dataset, composed of 925 observations distributed in the three case studies.

2.1 Data acquisition and aerial photogrammetry

The RGB images, acquired from a UAS flight over selected rivers, serve as input data for deriving in-water radiometric behaviour and surface model reconstruction through the photogrammetric procedure. Standard aerial photogrammetry workflow was applied, including ground control points measurements on-field and post-processing based on SfM and residual minimization. COTS quadricopters with an embedded imaging system were used, assuring lateral and longitudinal overlaps within frames of 80% in both directions. The UAS were similar for each case study, produced by the same firm, although mounting different optical cameras (FC6360 and FC6310R). All the drones used were equipped with multi-constellation and multi-frequency GNSS receivers that allow accurate positioning of the cameras' frames and the direct georeferencing of the photogrammetric block. Table 1 provides information about camera systems. The details regarding the georeferencing procedure and the residual errors on the GCP are reported in Section 3. The position coordinates (Easting, Northing, Height in UTM WGS 84) of each point belonging to the analyzed river sections were used to extract the radiometric pixel values of each band from the orthomosaic product and elevation information from the digital surface model.

Camera model	FC6310R	FC6360
Sensor	CMOS 1”	CMOS 1/2.9”
Bands	RGB – 8 bit	RGB - 8 bit. Red, Green, Blue, Red-Edge, NIR – 16 bit
Pixels	20 MP	2.08 MP each
Resolution	5472x3648	1600x1300
Focal length	8.8 mm	5.74 mm
HFOV	84.8°	62.7°

Table 1. Technical specification of optic image systems.

2.2 Feature extraction and data preparation

The dataset preparation is a fundamental step in NN. Considering the aims of this work in using UAS photogrammetric products to estimate shallow-water depths of Piedmont Rivers, three different test sites with peculiar characteristics for the interested region were selected. In those areas, direct measurements were made (RGB images, coordinates of ground points, riverbank depths), and from them, meaningful synthetic features were extracted:

1) Riverbank depths: river bottom depth measured directly through vessel-mounted Acoustic Doppler Current Profiler (ADCP) system, whose position in time is obtained from GNSS observations. A multi-constellation, multi-frequency receiver mounted on the vessel acquires the raw observations throughout the ADCP’s operational lifetime. These measurements are then processed to obtain a millimetre position estimate through the relative method.
2) Depth of the river bottom in a given cross-section $\boldsymbol{s}$, estimated by differentiating between the height of the river surface ($\mathrm{H\_DSM}_{s,1}$) and the height of the river bottom at a given point $\boldsymbol{i}$ extracted from the DSM ($\mathrm{H\_DSM}_{s,i}$). Through a stop-and-go NRTK survey, several points on the river bottom are measured with a pole-mounted GNSS receiver. The first measured point of each section coincides with the shoreline and provides the reference elevation to be subtracted to obtain the derived depth (Eq. 1).

$$\mathrm{Depth\_DSM}_{s,i} = \mathrm{H\_DSM}_{s,1} - \mathrm{H\_DSM}_{s,i} \qquad (1)$$

3) Radiometric features: Data array of normalized digital number values related to the three optical sensor bands (R, G, B), expressed in 8bit and extracted at georeferenced and identifiable points.
4) RGB bands derived indices: ratio between digital number values of R, G, B bands and Normalized Difference Turbidity Index (NDTI) as defined in (Lacaux et al., 2007).

The extracted features are reported in Table 2 with the relative description and formula.
The final dataset array has been prepared setting East, North and Height values as indices to maintain the spatiality of the information. Neural networks generally perform better if input and output variables are scaled. Then, each input feature was scaled using scikitlearn preprocessing MinMaxscaler (Pedregosa et al., 2011), which resize each feature on the minimum and maximum values, and the dependent variable (Depth_real) was scaled too.
The data of “Pellice” and “Orco” were used to train and internal testing the model (input dataset), while the data “Dora Riparia” case study were used as the unseen test dataset. The dependent variable constituted the Y dataset and the X dataset’s remaining variables.
The input dataset was an 805x11 matrix, Figure 2, which was split into test (20% observations, 563) and training (80% observations, 242) datasets.

Acronyms	Name and description	Formula
R	The red band of the DJI CMSO sensor	/
G	The green band of the DJI CMOS sensor	/
B	The blue band of the DJI CMOS sensor	/
NDTI	Normalized Difference Turbidity Index	$\frac{(\mathrm{Red}-\mathrm{Green})}{(\mathrm{Red}+\mathrm{Green})}$
R/G	Ratio between Red and Green	$\frac{\mathrm{Red}}{\mathrm{Green}}$
R/B	Ratio between Red and Blue	$\frac{\mathrm{Red}}{\mathrm{Blue}}$
G/R	Ratio between Green and Red	$\frac{\mathrm{Green}}{\mathrm{Red}}$
G/B	Ratio between Green and Blue	$\frac{\mathrm{Green}}{\mathrm{Blue}}$
B/R	Ratio between Blue and Red	$\frac{\mathrm{Blue}}{\mathrm{Red}}$
B/G	Ratio between Blue and Green	$\frac{\mathrm{Blue}}{\mathrm{Green}}$
Depth	Riverbank Depth	/

Table 2. Indices and bands compose the input dataset.

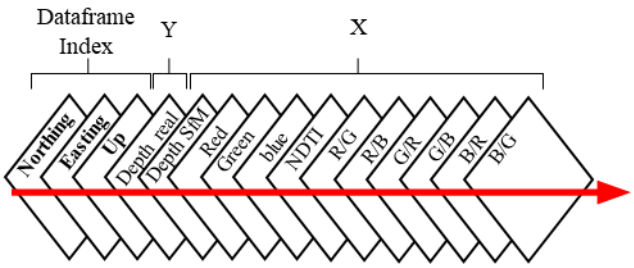

Figure 2. the input dataset.

2.3 Multilayer perceptron (MLP) Neural Network

The ANNs are mathematical models inspired by human brains’ biological neural networks functioning. ANNs are composed of layers of artificial neurons (individual operating units). An ANN model commonly involves an input layer and an output layer, but it can also contain one or more hidden layers. Artificial neural networks with multiple layers hierarchically organized between the input and output layers are called Deep Neural Networks (DNNs) (Schmidhuber, 2015). The hidden layers of DNNs are connected to each other in an a cyclic graph where the output of hidden layer i is the input of hidden layer i+1. The output layer is the last, and it generates the network’s output. This peculiar organization in layers makes DNNs particularly able to synthesize the input data and represent them with increasing levels of abstraction. Commonly, the higher the number of layers, the better the DNN can learn the fine-scale features in high-dimensional problems (Schmidhuber, 2015).
The most popular DNN are the multilayer perceptron (MLP) networks, in which the propagation rule happens through the internal computation of the weighted inputs, adding the bias term. Neurons connections towards the same level are not allowed. Once an ANN is trained, it can process patterns through forward propagation. The universal approximation theorem by (Hornik,

1991) asserts that an MLP with only one hidden layer can approximate any continuous function that maps ranges of real numbers to a range of real numbers.
In this work, the implementation of the neural network was realized in Python using the deep learning library Keras with TensorFlow backend (Abadi et al., 2016). The NN is a 3-layer MLP model with one hidden layer (Figure 3). The Rectified Linear Unit (ReLU) and sigmoid activation functions were added to the ANN layers to bring non-linear properties to the network; else, the output would be a linear function of the input (Larochelle et al., 2009). The dimension of the input layer is 11, and the weights are initialized to small Gaussian random values (kernel initializer 'Normal'). A kernel regulizers, L1 and L2, were added to reduce the overfitting. The applied optimizer to update weights in the network is the Adaptive Moment Estimation (Adam) search technique. The loss function, which evaluates the model used by the optimizer to navigate the weights, is the mean squared error between the predicted output and the target output.
The Mean Squared Error (MSE) loss was selected for the regression. The network was trained on the scaled training dataset ("Orco" and "Pellice" datasets) and then fitted with 90 epochs. Finally, the permutation importance was measured using the eli5 python library (Fan et al., 2019).

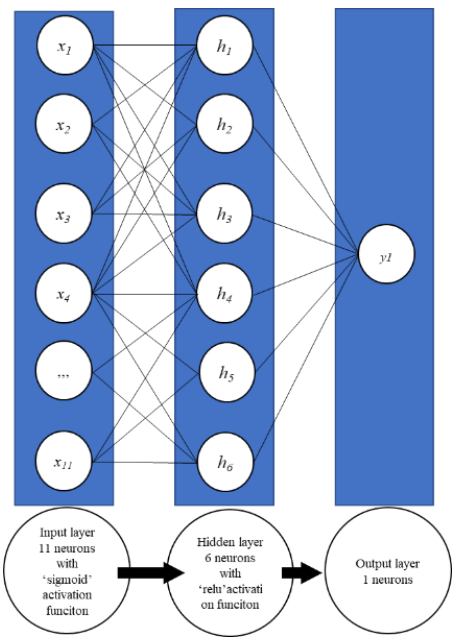

Figure 3. ANN structure.

2.4 Validation

The r-squared value between the predicted and real depths was computed for the test and train datasets. Also, the Mean Absolute Error (MAE) and the Root Mean squared error (RMSE) on the test dataset, were calculated respectively as:

$$MAE = \frac{\sum_{i=1}^{n}|y_i - x_i|}{n} \quad (2)$$

$$RMSE = \sqrt{\frac{\sum_{i=1}^{n}(y_i - x_i)^2}{n}} \quad (3)$$

Where y_i is the prediction and x_i the true value of n observations. The model was applied to the unseen dataset, "Dora Riparia", and the same metrics were computed and evaluated to check its ability to generalize.

3. CASE STUDY

3.1 Case Study 1: Dora Riparia River

One of the three data acquisitions was performed in northwest Italy, along the Dora Riparia river, which starts in the Cottian Alps and, flowing for about 100 kilometres through the Susa valley, ends in Torino as a tributary of the Po River. The analyzed stretch of river is about 1600 m long and is placed at 1000 m a.s.l. in the town of Salbertrand, in Torino province (45.074000 N, 6.892200 E). Limited slopes and a sinuous-meandering planimetry interrupted by multithread reaches with islands and disconnected terraces characterize the Dora Riparia River in the study stretch. From a geological point of view, the area is characterized by alluvial deposits and stratified sediment deposits of gravel and gravel-sandy, with rounded and finding pebbles and the presence of silty sand.
The Dora Riparia river flow is subject to considerable seasonal variations with the risk of floods in case of violent rainfall, such as the disastrous flood that occurred in October 2000 (over 700 m^3/s in Torino), which flooded the close by cities of Susa, Bussoleno and some districts of Torino. Dora Riparia River is constantly monitored and object of river engineering actions (Pontoglio et al., 2021), and such activities require detailed information regarding the river geomorphology.
The data for the analysis were collected in July 2020. To obtain georeferenced orthomosaic and DSM of the riverbed and banks the DJI P4 multispectral drone (Table 1) with RTK GNSS embedded receiver (Leica GS 18 model) was used, performing a planned flight at 90 meters above the ground level. The flights covered 0.78 km2 and provided 1066 frames with a 4.5 cm average ground sample distance (GSD). Moreover, 29 GCP were measured using GNSS NRTK technique, mounting a multi-frequency, multi-constellation receiver on a pole. With the same technique, seven cross-sections along the river for a total of 120 points and 56 points spread all over the river stretch were measured, extracting East, North and Height coordinates for 176 points (Figure 4).

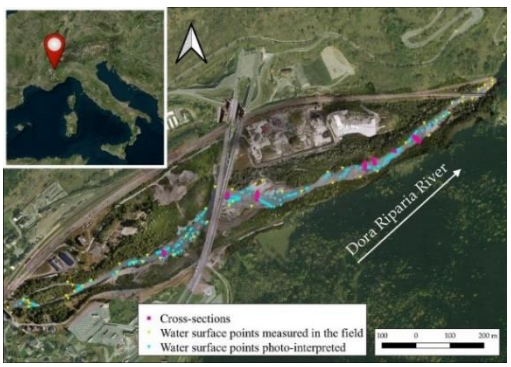

Figure 4. Dora Riparia orthomosaic map. The magenta squares indicate the cross-sections, blue triangles the water surface points manually identified from the orthophoto and yellow triangles the water surface points measured in the field.

The Height above the sea level was then used to compute the riverbank depth using Eq. 1. At the end of the photogrammetric processing, the orthomosaic and DSM resolution was 4 cm with an overall Root Mean Square Error (RMSE) of 2 cm on the check points.

3.2 Case Study 2: Orco River

The second case study is the Orco River, another tributary stream of Po River located in Northern Italy. This river has a slope

ranging from 0.0015 and 0.007. The sediment deposits contain course sand and pebbles. It performs a sinuous-meandering track interrupted by multithread reached with islands and disconnected terraces. The analyzed area is about 6 Km^2 in the section between Foglizzo and Chivasso (45.206899 N, 7.836887 E), at 262 m a.s.l. The data, acquired in February 2019, were part of a major multi-temporal study and monitoring activity due to the attention generated by flood events of significant impact.
Similarly to case study 1, an aerial photogrammetric survey was performed and post-processed to obtain high-resolution orthomosaic and DSM. In this case, the UAV data acquisition was performed with the DJI Phantom 4 RTK drone, with similar flight parameters to those used for the previous case study acquiring 486 images at 50 meters above the ground, assuring a ground resolution of the products of 1,25 cm/pix. 13 GCP, measured again with NRTK technique, has been used for refinement and georeferencing with an overall RMSE of 1,4 cm. Five bathymetric sections in low depth portions of the river were manually measured for 81 ground points with an accuracy of 1.4 cm (Figure 5).

Figure 5. Orco river orthomosaic map. The red lines indicate the cross-sections measured with GNSS, while the green triangles are the GCP used in the photogrammetric procedure.

3.3 Case Study 3: Pellice River

The third case study is located in northwest Italy, along the Pellice River, which springs from the Cottian Alps and, flowing for about 53 km, ends as a tributary of the Po River, at the Po-Pellice confluence park. The analyzed stretch of the river is about 200 m long and is placed at 247 m a.s.l. near the town of Faule, in Cuneo province (44.48912 N, 7.33338 E). The trail has the typical characteristics of a valley bottom stream: large quiet areas interspersed with streams and scrapes, small undulations, and the landscape is typical of the Piedmont countryside.
Numerous fish species inhabit this confluence and move up the Pellice River, especially in the winter and spring months, including the Marbled Trout (Salmo (t.) marmoratus), which nests in these waters and is being studied and safeguarded by the Fauna and Flora Protection Service of the Metropolitan City of Turin.
The data for the analysis were collected in February 2021. As for case studies 1 and 2, the features for the NN were derived from the aerial photogrammetric products (i.e. georeferenced Orthomosaic and DSM), but the riverbed measurements were acquired directly through vessel-mounted Acoustic Doppler Current Profiler (ADCP) system (Figure 6). The ADCP measures were georeferenced and synchronized with a GNSS receiver mounted on the vessel acquiring data at 1 Hz. This allows to associate the ADCP depth information with the vessel trajectory and therefore extract the coordinates of the points. In particular, the river depth was measured for 726 points along the river, along a trajectory that reproduced 14 cross-sections (Figure 7).

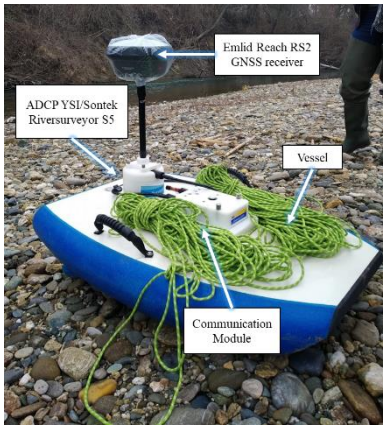

Figure 6. ADCP mounted on the mobile vessel.

Regarding the photogrammetric part, 369 images were acquired in nadiral configuration from the commercial DJI phantom 4 RTK UAV which mounts a CMOS sensor of 1" with 20 megapixels. The UAV flew 40 m above the ground. The flight was manually operated, with lateral and longitudinal overlaps within the frames of 80% in both directions. The flights covered a river stretch of about 300 m. The photogrammetric processing was performed using 10 GCP for georeferencing and image align refinement. The points were measured in real-time with NRTK techniques providing control coordinates with a cm-level accuracy. After the SfM and orientation refinement, the final overall ground resolution of the products was 6.53 mm/px, and the overall GCP RMSE was 1,5 cm.

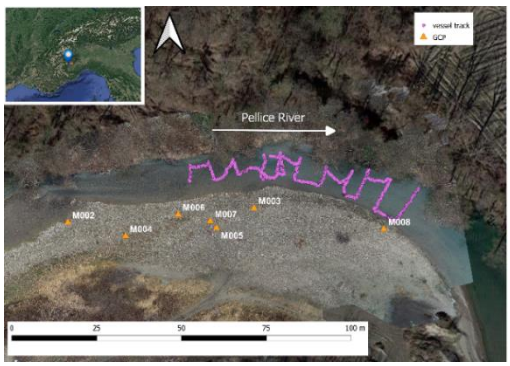

Figure 7. Pellice river orthomosaic map. The orange triangles represent the GCP measured with GNSS receiver, while the purple dots are the points extracted by the vessel-track.

Table 3 summarizes the information relates to the photogrammetric survey for each case study.

River	Dora Riparia	Orco	Pellice
Date	27 Jul 2020	28 Feb 2019	22 Feb 2021
Average height (m)	88	50	40
Average GSD (cm)	4.5	1.25	0.65
Area (km^2)	0.78	6	0.02
Number of images	1066	486	369
GCP RMSE (cm)	2	1.4	1.5
Orthomosaic resolution (cm)	4	1	1
DSM resolution (cm)	4	1	1

Table 3. Characteristics of the UAV campaign over the test area.

4. RESULTS

The neural network regressor performed with a 0.70 r-squared score on the test dataset and 0.77 on the training dataset. The MAE was 0.06 and the RMSE 0.08. The model loss on training and test datasets are plotted in Figure 8 and shows that the model converged around the 20 epochs and both train and test performance remained equivalent.

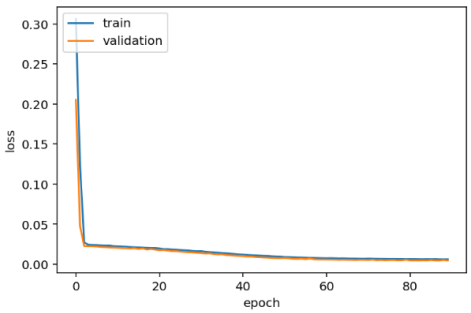

Figure 8. Model loss of training and test datasets.

Figure 9 represents the correctness of the prediction of test and training datasets. The plot indicates the real values on the abscissae and predicted values on the ordinates. Thus, the best scenario is when the observations are on the diagonal of the plot. This plot shows that the model better predicted high depths (>0.5 scaled values) than small depths.

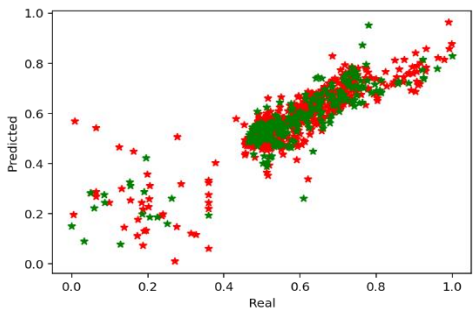

Figure 9. Plot of real and predicted train data (red stars) and test data (green stars). Real depth values are indicated on the abscissae and the predicted values in the ordinates.

A permutation importance analysis was realized to assess the relative role of each feature within the network (Table 4). The most influential features are the R/B, the Normalized Difference Turbidity Index and the R/G. The model was then applied to the unseen dataset (120 observations from the "Dora Riparia" case study), revealing a quite stable performance, indeed, the MAE is 0.08 m, and the RMSE is 0.10 m. Although the plot of the predicted and the real data shown in Figure 10 shows some incoherence.

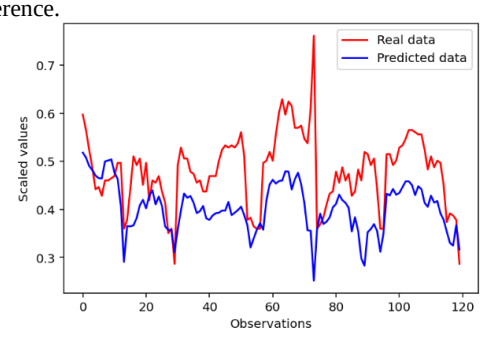

Figure 10. Real (red) and predicted (blue) data of the unseen dataset.

Importance +/- standard deviation	Feature
0.0031 ± 0.0004	R/B
0.0021 ± 0.0004	NDTI
0.0020 ± 0.0006	R/G
0.0015 ± 0.0002	B/R
0.0009 ± 0.0004	G/B
0.0006 ± 0.0001	G/R
0.0005 ± 0.0003	R
0.0004 ± 0.0001	B
0.0002 ± 0.0000	Depth_dsm
0.0000 ± 0.0000	B/G
-0.0000 ± 0.0000	G

Table 4. Results of the permutation analysis on the ANN model, considering the negative mean squared error measures.

5. DISCUSSION

In this section, we begin by reviewing the results presented in Section 4, including the limitations of the network in its current form. We then consider improving the model and creating a harmonized open dataset for bathymetry based on SfM.

General discussion

The present work aims to estimate the riverbed submerged topography of alpine rivers using NN and information derived from UAS photogrammetry. The training dataset comprises two case studies, namely Pellice and Orco rivers, both located in north-western Italy, and one unsees case study, the Dora Riparia river. The SfM-derived information is RGB orthomosaics and the digital elevation model, generated through a standard workflow and resulting in highly accurate products.
The developed model, although simple, fits well the training dataset, 0.77 r-squared, and loose little precision on the training dataset, 0.70 r-squared. The performance and stability of the model can be appreciated in Figure 8, where the plot of the loss function shows a quick convergence and equivalent performances of the model on the train and test datasets. Being smaller than 0.10 m, the MAE and RMSE are acceptable for the application since 0.10 m equals the RTK positioning accuracy and represents the average size of the bedrock of the analyzed rivers. Figure 9 illustrates a good performance for deepwater (more than 0.5 scaled depth values) and worse for swallow waters. This behaviour can be ascribable to the morphology of bank rivers; indeed, the selected sites have pebbles along the banks and seral rocks and emerging sandbanks in the riverbed.
Moreover, at the same depth, vegetation in shallow water areas is a source of spectral differences from the bedrock. The NN might not be able to model these aspects correctly. In fact, the model is trained on 563 observations, a relatively small dataset for DNNs that are generally applied on larger datasets (at least more than 500 observations), not available for this study. Additional data are needed to model alpine rivers fully. The limitations of the small dataset are also testified by the generalization capability of the NN. The RMSE and MAE computed on the unseen dataset are larger than those measured on the training data, respectively 0.10m and 0.08m, and the RMSE only fulfils the minimum requirements for bathymetry.
While the error metrics have acceptable values, the forecast graph is slightly different from the actual data, as Figure 10 reports. The prediction underestimated part of the observations and presented evident outliers in correspondence of observations 75 and 90,

which are a clue of bias in the model. This is another symptom of a too-small dataset to produce precise results. The poor number of training observations might have led the model to overfit the data; despite a kernel size to each hidden layer being added to avoid overfitting. Although, the loss curves of training and test measured on the mean squared error do not indicate strong overfitting (Figure 8).

A deeper look into the model unveils the importance of the R/B and NDTI features, which are highly ranked in permutation analysis. Based on the literature, a continuous and constant correlation between the actual depth and the apparent depth estimated with the SfM technique was expected. Still, the photogrammetric depth has a 0.0002 permutation value, meaning it has very little influence on the regressor performances. The minmax scaling method, which scales each feature according to the internal minimum and maximum values, might impact the relation between features. The scientific community knows the strong influence of scaling methods on NN and machine learning models, and further investigation on scaling methods should be carried out for this specific application.

Besides the accuracy of the model, the structure of the input dataset requires some specific considerations. Most of the observations are part of the "Pellice" case study (653 observations versus 69 of Orco river). Consequently, the characteristics of Pellice river have a major influence on the model structure than Orco river, which might affect the ability of the model to generalize.

Also, the methodology used for the real depths measures might have introduced some bias because the ground truth data were acquired partly with the GNSS receiver and pole and partly with the ADCP mounted on a vessel. The two methods receive both RTK corrections and achieve the same degree of accuracy and precision. However, two aspects should be considered and possibly analyzed. The pointed pole penetrates more in the bottom of the bed, especially if this is constituted of sands and silts. In general, it provides less dense data than the ADCP that acquires with greater precision and frequency.

On the other hand, the ADCP depth measurements could be affected by slightly time-synchronization errors with respect to the GNSS time; consequently, a shift between the pixel radiometric value and the depth information may occur. Another noteworthy aspect related to the data collection methodology is measuring the water surface to calculate depth. In the case of the ADCP, the water surface is measured by subtracting from the RTK Up component, measured by the GNSS receiver onboard, the offset of the support and the sinking of the vessel itself. Instead, the water surface for GNSS measurements with the pole is made manually according to the surveyor's interpretation. Both methodologies are validated and reliable but still different, and no comparison between the two methods has been realized for this work. We intend to analyze this aspect in the following stages of the study.

Improving the ANN

The ANN performs reasonably well and lays the foundation for further research on neural networks to develop a more comprehensive and extended model to correct bathymetry from UAS photogrammetry. The main limitation is related to the small and unbalanced dataset; we believe that by adding observations from different case studies, the model would better generalize. Of course, we expect to need to modify the network structure by adding observations. We will continue to collect data to feed our model.

We believe that today many researchers in the field of hydraulics and land morphology have available similar data to ours, collected with RGB sensors and profilers or GNSS receivers. We intend to seek the help of the scientific community to carry out this research. First of all, we would like to create a shared database where our data will be available and where anyone can make their data public. The mutual exchange of information and open data benefit different research groups worldwide.

6. CONCLUSIONS

This investigation aimed to assess the effectiveness of the NN-based model for the correction of water refraction in shallow inland alpine rivers using information extracted from SfM data. The proposed neural network is straightforward, but we aim to improve it in terms of datasets and from a structural point of view. More data would help to establish a greater degree of accuracy on riverine bathymetry from NNs. The future activities are indeed addressed in this way.

REFERENCES

Abadi, M. *et al.* (2016) 'TensorFlow: Large-Scale Machine Learning on Heterogeneous Distributed Systems', *arXiv:1603.04467*. Available at: http://arxiv.org/abs/1603.04467 (Accessed: 6 December 2021).

Agrafiotis, P. *et al.* (2019) 'DepthLearn: Learning to Correct the Refraction on Point Clouds Derived from Aerial Imagery for Accurate Dense Shallow Water Bathymetry Based on SVMs-Fusion with LiDAR Point Clouds', *Remote Sensing*, 11(19), p. 2225. Available at: https://doi.org/10.3390/rs11192225.

Balletti, C. *et al.* (2015) 'UNDERWATER PHOTOGRAMMETRY AND 3D RECONSTRUCTION OF MARBLE CARGOS SHIPWRECK', *The International Archives of the Photogrammetry, Remote Sensing and Spatial Information Sciences*, XL-5/W5, pp. 7–13. Available at: https://doi.org/10.5194/isprsarchives-XL-5-W5-7-2015.

Burgazzi, G. *et al.* (2021) 'Effect of microhabitats, mesohabitats and spatial position on macroinvertebrate communities of a braided river', *Journal of Ecohydraulics*, 6(2), pp. 95–104. Available at: https://doi.org/10.1080/24705357.2021.1938254.

Calantropio, A., Chiabrando, F. and Auriemma, R. (2021) 'PHOTOGRAMMETRIC UNDERWATER AND UAS SURVEYS OF ARCHAEOLOGICAL SITES: THE CASE STUDY OF THE ROMAN SHIPWRECK OF TORRE SANTA SABINA', *The International Archives of the Photogrammetry, Remote Sensing and Spatial Information Sciences*, XLIII-B2-2021, pp. 643–650. Available at: https://doi.org/10.5194/isprs-archives-XLIII-B2-2021-643-2021.

Carbonneau, P.E., Lane, S.N. and Bergeron, N. (2006) 'Feature based image processing methods applied to bathymetric measurements from airborne remote sensing in fluvial environments', *Earth Surface Processes and Landforms*, 31(11), pp. 1413–1423. Available at: https://doi.org/10.1002/esp.1341.

Dietrich, J.T. (2017) 'Bathymetric Structure-from-Motion: extracting shallow stream bathymetry from multi-view stereo photogrammetry', *Earth Surface Processes and Landforms*, 42(2), pp. 355–364. Available at: https://doi.org/10.1002/esp.4060.

Fan, A. *et al.* (2019) 'ELI5: Long Form Question Answering', in *Proceedings of the 57th Annual Meeting of the Association for Computational Linguistics*. *Proceedings of the 57th Annual*

Meeting of the Association for Computational Linguistics, Florence, Italy: Association for Computational Linguistics, pp. 3558–3567. Available at: https://doi.org/10.18653/v1/P19-1346.

Geyman, E.C. and Maloof, A.C. (2019) 'A Simple Method for Extracting Water Depth From Multispectral Satellite Imagery in Regions of Variable Bottom Type', *Earth and Space Science*, 6(3), pp. 527–537. Available at: https://doi.org/10.1029/2018EA000539.

Ghorbanidehno, H. *et al.* (2021) 'Deep learning technique for fast inference of large-scale riverine bathymetry', *Advances in Water Resources*, 147, p. 103715. Available at: https://doi.org/10.1016/j.advwatres.2020.103715.

Hornik, K. (1991) 'Approximation capabilities of multilayer feedforward networks', *Neural Networks*, 4(2), pp. 251–257. Available at: https://doi.org/10.1016/0893-6080(91)90009-T.

Ioli, F. *et al.* (2020) 'EVALUATION OF AIRBORNE IMAGE VELOCIMETRY APPROACHES USING LOW-COST UAVS IN RIVERINE ENVIRONMENTS', in *The International Archives of the Photogrammetry, Remote Sensing and Spatial Information Sciences. XXIV ISPRS Congress, Commission II (Volume XLIII-B2-2020) - 2020 edition*, Copernicus GmbH, pp. 597–604. Available at: https://doi.org/10.5194/isprs-archives-XLIII-B2-2020-597-2020.

Kaloop, M.R. *et al.* (2021) 'Hybrid Artificial Neural Networks for Modeling Shallow-Water Bathymetry via Satellite Imagery', *IEEE Transactions on Geoscience and Remote Sensing*, pp. 1–11. Available at: https://doi.org/10.1109/TGRS.2021.3107839.

Lacaux, J.-P. *et al.* (2007) *Classification of ponds from high-spatial resolution remote sensing: Application to Rift Valley Fever epidemics in Senegal*. Available at: /paper/Classification-of-ponds-from-high-spatial-remote-to-Lacaux-Tourre/dde8fa0f53c86ea97c9df70f0afa063acdcf5970 (Accessed: 8 June 2020).

Larochelle, H. *et al.* (2009) 'Exploring strategies for training deep neural networks', *Journal of Machine Learning Research*, 10, pp. 1–40.

Legleiter, C.J., Roberts, D.A. and Lawrence, R.L. (2009) 'Spectrally based remote sensing of river bathymetry', *Earth Surface Processes and Landforms*, 34(8), pp. 1039–1059. Available at: https://doi.org/10.1002/esp.1787.

Lyzenga, D.R. (1978) 'Passive remote sensing techniques for mapping water depth and bottom features', *Applied Optics*, 17(3), pp. 379–383. Available at: https://doi.org/10.1364/AO.17.000379.

Makboul, O. *et al.* (2017) 'Performance Assessment of ANN in Estimating Remotely Sensed Extracted Bathymetry. Case Study: Eastern Harbor of Alexandria', *Procedia Engineering*, 181, pp. 912–919. Available at: https://doi.org/10.1016/j.proeng.2017.02.486.

Mancini, F. *et al.* (2020) 'The impact of innovative and emerging technologies on the surveying activities', *Applied Geomatics*, 12(1), pp. 1–2. Available at: https://doi.org/10.1007/s12518-020-00302-x.

Mandlburger, G. *et al.* (2021) 'BathyNet: A Deep Neural Network for Water Depth Mapping from Multispectral Aerial Images', *PFG – Journal of Photogrammetry, Remote Sensing and Geoinformation Science*, 89(2), pp. 71–89. Available at: https://doi.org/10.1007/s41064-021-00142-3.

de Pauli, S.T.Z., Kleina, M. and Bonat, W.H. (2020) 'Comparing Artificial Neural Network Architectures for Brazilian Stock Market Prediction', *Annals of Data Science*, 7(4), pp. 613–628.

Pedregosa, F. *et al.* (2011) 'Scikit-learn: Machine Learning in Python', *Journal of Machine Learning Research*, 12(85), pp. 2825–2830.

Pontoglio, E. *et al.* (2020) 'Bathymetric Detection of Fluvial Environments through UASs and Machine Learning Systems', *Remote Sensing*, 12(24), p. 4148. Available at: https://doi.org/10.3390/rs12244148.

Pontoglio, E. *et al.* (2021) 'Automatic Features Detection in a Fluvial Environment through Machine Learning Techniques Based on UAVs Multispectral Data', *Remote Sensing*, 13(19), p. 3983. Available at: https://doi.org/10.3390/rs13193983.

Rossi, L., Mammi, I. and Pelliccia, F. (2020) 'UAV-Derived Multispectral Bathymetry', *Remote Sensing*, 12(23), p. 3897. Available at: https://doi.org/10.3390/rs12233897.

Schmidhuber, J. (2015) 'Deep Learning in Neural Networks: An Overview', *Neural Networks*, 61, pp. 85–117. Available at: https://doi.org/10.1016/j.neunet.2014.09.003.

Slocum, R.K., Parrish, C.E. and Simpson, C.H. (2020) 'Combined geometric-radiometric and neural network approach to shallow bathymetric mapping with UAS imagery', *ISPRS Journal of Photogrammetry and Remote Sensing*, 169, pp. 351–363. Available at: https://doi.org/10.1016/j.isprsjprs.2020.09.002.

Stumpf, R.P., Holderied, K. and Sinclair, M. (2003) 'Determination of water depth with high-resolution satellite imagery over variable bottom types', *Limnology and Oceanography*, 48(1part2), pp. 547–556. Available at: https://doi.org/10.4319/lo.2003.48.1_part_2.0547.

Vélez-Nicolás, M. *et al.* (2021) 'Applications of Unmanned Aerial Systems (UASs) in Hydrology: A Review', *Remote Sensing*, 13(7), p. 1359. Available at: https://doi.org/10.3390/rs13071359.

Wang, Y. *et al.* (2007) 'Study on Remote Sensing of Water Depths Based on BP Artificial Neural Network.' Available at: https://aquadocs.org/handle/1834/5850 (Accessed: 4 November 2021).

Woodget, A.S. *et al.* (2015) 'Quantifying submerged fluvial topography using hyperspatial resolution UAS imagery and structure from motion photogrammetry', *Earth Surface Processes and Landforms*, 40(1), pp. 47–64. Available at: https://doi.org/10.1002/esp.3613.